ACD15, ACD21 and SLN regulate accumulation and mobility of MBD6 to silence genes and transposable elements.

Authors: Brandon A. Boone[1,2,6], Lucia Ichino[1,2,6], Shuya Wang[1,2], Jason Gardiner[2,7], Jaewon Yun[2], Yasaman Jami-Alahmadi[3], Jihui Sha[3], Cristy P. Mendoza[2], Bailey J. Steelman[2], Aliya van Aardenne[2], Sophia Kira-Lucas[2], Isabelle Trentchev[2], James A. Wohlschlegel[3], Steven E. Jacobsen[1,2,3,4,5]*

Affiliations:

[1]Molecular Biology Institute, University of California Los Angeles, Los Angeles, CA 90095, USA

[2]Department of Molecular, Cell and Developmental Biology, University of California Los Angeles, Los Angeles, CA 90095, USA

[3]Department of Biological Chemistry, University of California Los Angeles, Los Angeles, CA 90095, USA

[4]Eli and Edyth Broad Center of Regenerative Medicine and Stem Cell Research, University of California Los Angeles, Los Angeles, CA 90095, USA

[5]Howard Hughes Medical Institute (HHMI), UCLA; Los Angeles, CA 90095, USA

[6]These authors contributed equally

[7]Translational Plant Biology, Department of Biology, Utrecht University, 3584CH, Utrecht, The Netherlands

*Corresponding author. Email: jacobsen@ucla.edu (S.E.J)

Abstract: DNA methylation mediates silencing of transposable elements and genes in part via recruitment of the Arabidopsis MBD5/6 complex, which contains the methyl-CpG-binding domain (MBD) proteins MBD5 and MBD6, and the J-domain containing protein SILENZIO (SLN). Here we characterize two additional complex members: α-crystalline domain containing proteins ACD15 and ACD21. We show that they are necessary for gene silencing, bridge SLN to the complex, and promote higher order multimerization of MBD5/6 complexes within heterochromatin. These complexes are also highly dynamic, with the mobility of complex components regulated by the activity of SLN. Using a dCas9 system, we demonstrate that tethering the ACDs to an ectopic site outside of heterochromatin can drive massive accumulation of MBD5/6 complexes into large nuclear bodies. These results demonstrate that ACD15 and ACD21 are critical components of gene silencing complexes that act to drive the formation of higher order, dynamic assemblies.

One-Sentence Summary: Arabidopsis ACD21 and ACD15 drive accumulation of MBD5/6 complex silencing assemblies at methyl-CG sites and recruit SLN to maintain protein mobility in these assemblages.

Main Text

Eukaryotic organisms must properly localize macromolecules within cells to maintain homeostasis. Membrane bound organelles serve this purpose, but recent discoveries have revealed the existence of membrane-less organelles or compartments(*1–3*). Often referred to as biological condensates, liquid-liquid phase separated (LLPS) condensates, or supramolecular assemblies, these compartments such as stress granules, p-granules, heterochromatin, and the nucleolus concentrate proteins and nucleic acids to facilitate specific and efficient processes(*4–7*). If not properly controlled, the accumulation of these protein assemblies can lead to aggregates with detrimental impacts on cellular homeostasis and disease, yet how cells regulate these assemblies remains unclear(*3*, *8*, *9*). Molecular chaperones, such as heat shock proteins (HSPs), serve highly conserved roles to regulate the solubility, folding, and aggregation of proteins within cells, making them obvious candidates for the regulation of biological condensates(*10–14*). Small HSPs (sHSPs) use their conserved α-crystalline domains (ACD) to form dimers which then create large and dynamic oligomeric assemblies that act as first line of defense against protein aggregation via a "holdase" activity(*14*). sHSPs further recruit J-domain containing proteins (JDPs) which act as co-chaperones for HSP70 proteins to maintain protein homeostasis (*14–17*). Both sHSPs and JDP/HSP70 pairs have been shown to associate with and regulate disease related cellular condensates across species(*18–21*).

In *Arabidopsis thaliana*, pericentromeric heterochromatin is organized into compartments called chromocenters that are chromatin dense regions containing most of the DNA methylated and constitutively silenced TEs and genes, as well as heterochromatic proteins such as DNA methylation binding complexes (*13*, *22–26*). Previous work has shown that multiple Arabidopsis DNA methylation binding complexes silence or promote expression of genes through recruitment of molecular chaperones with unknown functions (*27–29*). For example, MBD5 and MBD6 redundantly silence a subset of TEs and promoter-methylated genes via recruitment of SLN, a JDP. MBD5/6 also interact with two ACD containing proteins called ACD15.5/RDS2 and ACD21.4/RDS1, hereafter referred to as ACD15 and ACD21(*29–31*). While ACD15 and ACD21 have been implicated in silencing of a transgene reporter, their specific chromatin functions remain unknown (*31*). Here we demonstrate that ACD15 and ACD21 are necessary and sufficient for the accumulation of high density MBD6 at methylated CG sites to silence genes and TEs, while also bridging SLN to MBD5/6 to maintain the high mobility of all complex components. We further demonstrate that MBD5/6 complex assemblies can be formed at discrete foci outside of chromocenters, in an ACD15 and ACD21 dependent manner, to cause gene silencing.

ACD15 and ACD21 colocalize with MBD5 and MBD6 genome-wide and are essential for silencing.

We previously observed that MBD5, MBD6 and SLN pulled-down two ACD containing proteins named ACD15 and ACD21 (*29*). To investigate their binding patterns on chromatin, we performed Chromatin Immunoprecipitation sequencing (ChIP-seq) of FLAG-tagged ACD15 and ACD21. We observed that all five proteins colocalized genome-wide, and none of them appeared to have truly unique ChIP-seq peaks, suggesting that they could be recruited to DNA together as a complex (Fig. 1A-B, S1A). Furthermore, ACD15 and ACD21 showed a non-linear correlation with meCG density similar to MBD6 and SLN(*29*) suggesting that MBD5/6 complex members all accumulate preferentially at high density meCG sites (Fig. 1C).

To test whether ACD15 and ACD21 are required for silencing we generated *acd15* and *acd21* single mutants, an *acd15 acd21* double mutant, and an *acd15 acd21 sln* triple mutant via CRISPR/Cas9 (fig. S1B). RNA-seq analysis revealed that all mutants showed very similar

transcriptional derepression patterns at DNA methylated genes and TEs as compared to *mbd5 mbd6* and *sln* mutants (Fig. 1D-F, S1C-D). This includes the *FWA* gene which was previously shown to be silenced by the MBD5/6 complex (Fig. 1F) (*29*). These results demonstrate that ACD15 and ACD21 are critical components of the MBD5/6 complex required for silencing.

ACD15 and ACD21 bridge SLN to MBD5 and MBD6.

To determine the specific organization of the MBD5/6 complex, we performed IP-MS experiments using FLAG-tagged transgenic lines for each complex component in different mutant backgrounds (Fig. 2A, Table S1). In the wild type Col0 background, ACD15 and ACD21 pulled-down each other, MBD5, MBD6, SLN, and the same HSP70 proteins that were found to interact with the MBD5/6 complex previously (*29*) (Fig. 2A, Table S1). MBD5 and MBD6 pulled down peptides of ACD15 and ACD21 in the absence of SLN, while SLN did not pull down MBD5 and MBD6 in the absence of ACD15 and ACD21, suggesting that ACD15 and ACD21 bridge the interaction between MBD5/6 and SLN (Fig. 2A-B). Consistent with this model, ACD15 and ACD21 pulled down MBD5 and MBD6 in the *sln* mutant background, and SLN pulled down ACD15 and ACD21 in the *mbd5 mbd6* mutant background (Fig. 2A). ACD15 also pulled-down MBD5 and MBD6 but not SLN in the absence of ACD21, while ACD21 did not pull down MBD5 and MBD6 in the absence of ACD15 (Fig. 2A). These results suggest that the MBD5/6 complex is organized such that MBD5 or MBD6 interact with ACD15, ACD15 interacts with ACD21, and ACD21 interacts with SLN (*29*) (Fig. 2B).

To further study the organization and localization of MBD5/6 complex components we used live confocal imaging of root tips to determine the cellular localization of fluorescent-protein-tagged ACD15, ACD21, SLN, and MBD6. In wild-type plants, ACD15, ACD21, and SLN all showed clear nuclear localization which correlated strongly with nuclear MBD6 (Fig. 2C-E and S2A-C). ACD21, ACD15, and SLN all showed an increase in cytosolic signal in *mbd5 mbd6* mutant plants which was rescued by coexpressing MBD6, demonstrating that all members of the complex require genetically redundant MBD5 or MBD6 for proper nuclear localization (Fig. 2C-E). The reduction of nuclear localization of SLN is also consistent with previous ChIP-seq experiments showing loss of chromatin bound SLN in the absence of MBD5 and MBD6(*29*). ACD15 maintained nuclear localization and correlation with MBD6 in *acd15 acd21* and *sln* mutant plants whereas ACD21 lost nuclear localization and correlation with MBD6 in *acd15* and *acd15 acd21* mutants, but not in the *sln* mutant (Fig. 2C-D, S2D-G). Finally, SLN nuclear localization and correlation with MBD6 decreased in *acd15, acd21,* and *acd15 acd21,* mutant plants (Fig. 2E, S2H,I). These results demonstrate that ACD21 requires ACD15 for proper nuclear localization, while SLN requires both ACD15 and ACD21, consistent with the complex organization model suggested by IP-MS experiments (Fig. 2B).

We used the protein folding algorithm AlphaFold Multimer to predict protein-protein interactions within the MBD5/6 complex(*32*, *33*). AlphaFold Multimer confidently predicted that ACD15 interacts with MBD6 (or MBD5), that ACD15 interacts with ACD21, and that ACD21 interacts with SLN, all consistent with our experimental data from IP-MS and confocal microscopy (Fig. 2F). When given two copies of each member of the complex (MBD6, ACD15, ACD21, and SLN), AlphaFold Multimer also confidently predicted that ACD15 and ACD21 form a dimer of two heterodimers in the middle of the structure, suggesting that the MBD5/6 complex likely contains at least two copies of each protein (fig. S2J-L). This is consistent with previous results showing dimer formation by other ACD containing sHSPs (*34*). Given the genetic redundancy of MBD5 and MBD6, the complex would be predicted to contain a minimum of two MBD5s, two MBD6s, or one MBD5 plus one MBD6 (fig. S2L). In line with this prediction, we found that MBD5 and MBD6 pull-down each other in IP-MS data in wild-

type, but not in the *acd15 acd21* double mutant background, indicating that ACD15/ACD21 facilitate interaction between two MBD5/6 proteins (Fig. 2A, S2L).

ACD15, ACD21, and SLN regulate heterochromatic localization, accumulation, and dynamics of the MBD5/6 complex.

Given the known role of molecular chaperones in the regulation of protein complexes and aggregates (*35*), we hypothesized that ACD15, ACD21, and SLN may regulate the dynamics of MBD5/6 nuclear complexes. To test this, we measured the nuclear localization and mobility of MBD6 in root cells using live-cell, fluorescence, confocal microscopy. In wild-type and *mbd5 mbd6* mutant plants, MBD6 formed foci, which colocalized with ACD15, ACD21, and SLN foci (Fig. 3A-B, S3A). MBD6 foci also overlapped with DAPI-staining chromocenters, as previously shown when MBD6 was overexpressed in leaf cells (fig. S3B) (*36*). To measure the mobility of MBD6 protein we used fluorescence recovery after photobleaching (FRAP) experiments (*37*). FRAP in wild-type plants revealed that MBD6 moves rapidly within nuclei with a FRAP recovery half time ($t_{1/2}$) of ~3.60 seconds back into chromocenters after bleaching (Fig. 3C-D, S3D).

We next tested whether MBD6 nuclear distribution or mobility was altered in *sln* mutants. Although MBD6 formed a similar number of nuclear foci in *sln* compared to wild-type plants, these foci showed somewhat reduced fluorescence intensity, suggesting that MBD6 was accumulating less efficiently within heterochromatin (Fig. 3A, E, F). FRAP of MBD6 in *sln* mutant plants revealed a dramatic reduction in mobility and a lack of full recovery of signal post bleaching (Fig. 3C-D and S3D). Similar FRAP experiments on ACD15 and ACD21 nuclear foci showed that both were highly mobile in wild-type ($t_{1/2}$ of 3.63 and 4.30 seconds respectively), but were much less mobile and failed to recover full signal in *sln* mutant plants (Figure S3D-H), and also showed decreased fluorescence intensity of foci in *sln* compared to wild-type (fig. S3I-J). SLN thus regulates the mobility, and to a lesser extent the accumulation of the MBD5/6 complex.

Given the IP-MS, microscopy, and structure prediction results showing that ACD15 and ACD21 bridge the interaction between MBD6 and SLN we expected *acd15 acd21* mutants to alter the FRAP mobility of MBD6 in a manner similar to *sln* mutants. However, we found that the number of MBD6 foci were dramatically lower in *acd15 acd21* mutant plants compared to wild-type plants, with only occasional MBD6 foci observed (Fig. 3A, B, E). Instead, MBD6 nuclear signal in *acd15 acd21* mutant plants was more diffusely distributed across nuclei compared to either wild-type or *sln* plants (Fig. 3A). A decreased number of MBD6 foci and a lack of overlap of these foci with DAPI stained chromocenters was also observed in *acd15, acd21,* and *acd15 acd21 sln* mutant plants (Fig. 3A, fig. S3C). Thus, ACD15 and ACD21 are required for MBD6 to efficiently concentrate into nuclear foci. This effect was specific to ACD15 and ACD21 since loss of IDM3 (LIL), an ACD protein in the MBD7 complex (*28*), did not affect the MBD6 nuclear foci (fig. S3K-L).

We performed ChIP-seq on MBD6 in *acd15 acd21* mutant plants to quantify the impact on MBD6 chromatin localization. In wild-type plants, MBD6 localized to previously published MBD6 peaks(*29*) and showed a non-linear correlation with meCG density, displaying strong enrichment at highly dense methylated regions (Fig. 3G-I). However, MBD6 chromatin enrichment in *acd15 acd21* mutant plants, although not abolished, was decreased dramatically and showed much less preference for binding to high density meCG sites (Fig. 3G-I). Thus, while ACD15/ACD21 are not necessary for MBD6 to bind meCG sites, they are needed for high accumulation of MBD6 at high density meCG sites, which is consistent with the decrease of observable MBD6 foci in *acd* mutants (Fig. 3A-B).

Taken together, these results demonstrate that ACD15 and ACD21 are required for high level accumulation of MBD5/6 complexes in chromocenters and at high density meCG sites, while SLN regulates the mobility of these complexes to maintain dynamic recycling of proteins.

The StkyC domain of MBD6 is required for gene silencing and recruits ACD15 to the complex.

The AlphaFold-predicted structure of MBD6 reveals two structured domains, the MBD and a C-terminal domain of unknown function, as well as two intrinsically disordered regions (IDRs) (Figure 4A, and S4A). The C-terminal folded domain shares amino acid similarity with the C-terminus of two related MBD proteins, MBD5 and MBD7 (fig. S4B). This region of MBD7 has been termed the StkyC domain, and is the proposed binding site for the ACD containing IDM3 protein, which belongs to the same family as ACD15 and ACD21(*28*). This suggests that the StkyC of MBD6 would interact with ACD15, and indeed this interaction is confidently predicted by AlphaFold Multimer (Fig. 2F, S2J-K, S4A).

To experimentally determine what domains of MBD6 are necessary for gene silencing and chaperone interactions we first truncated the N-terminus (MBD6$^{N\Delta}$ (leaving amino acids 66-224)) or the C-terminus of MBD6 (MBD6$^{C\Delta}$ (leaving amino acids 1-146)) (fig. S4C). To test if these mutants are functional for silencing, we performed RT-qPCR of the *FWA* gene, a target of the MBD5/6 complex (Fig. 1F)(*29*), in *mbd5 mbd6* mutant plants expressing full-length or truncated MBD6 alleles. *FWA* derepression in *mbd5 mbd6* plants was rescued by full length MBD6-RFP or MBD6$^{N\Delta}$-RFP, but not by MBD6$^{C\Delta}$-RFP, showing that the middle IDR and/or the StkyC domain are required for MBD6 function (fig. S4D). MBD6$^{C\Delta}$ also showed a dramatic reduction in nuclear foci compared to full length MBD6, a phenotype similar to that observed in *acd15 acd21* mutants and consistent with loss of the ACD15 binding site (Fig. 4B-C, S4E).

To test if the StkyC domain was critical, we added back the StkyC domain (amino acids 167-224) to MBD6$^{C\Delta}$ (MBD6$^{C\Delta+StkyC}$). MBD6$^{C\Delta+StkyC}$ was able to rescue MBD6 nuclear foci counts, and complemented the derepression of *FWA* in the *mbd5 mbd6* mutant (Fig. 4B-E). Importantly, MBD6$^{C\Delta+StkyC}$ expressed in *acd15 acd21* mutant plants formed very few nuclear foci, similar to the low number of MBD6$^{C\Delta}$ foci in wild-type plants, demonstrating that foci localization rescue by the StkyC domain requires ACD15 and ACD21 (Fig. 4D).

To determine if the StkyC domain is responsible for localizing ACD15 and ACD21 to the MBD5/6 complex, we performed fluorescent protein colocalization experiments by co-expressing ACD21-CFP or ACD15-YFP with MBD6-RFP, MBD6$^{C\Delta}$-RFP, or MBD6$^{C\Delta+StkyC}$ RFP in *mbd5 mbd6* mutants. ACD15 and ACD21 both strongly correlated with full length MBD6 (Pearson correlation coefficient (*r)* of 0.96 and 0.86 respectively) and overlapped well with MBD6 signal across root nuclei, whereas ACD15 and ACD21 showed much weaker correlations with MBD6$^{C\Delta}$ (r = 0.67 and 0.46, respectively) and lost overlap with MBD6$^{C\Delta}$ nuclear signal (Fig. 4F-G and S4F-G). ACD15 and ACD21 also showed visibly higher cytosolic signal and lower nuclear signal when co-expressed with MBD6$^{C\Delta}$ in *mbd5 mbd6* (Fig. 4F-G and S4F-G). The addition of the StkyC domain (MBD6$^{C\Delta+StkyC}$) restored the correlation of ACD15 and ACD21 with MBD6 (r = 0.94 and 0.84 respectively), restored the overlap of ACD15 and ACD21 with MBD6 nuclear signal, and reversed the cytosolic localization of ACD15 and ACD21 (Fig. 4F-G and S3F-G).

To further test if ACD15 is needed for ACD21 to associate with MBD6$^{C\Delta+StkyC}$, we colocalized ACD15 and ACD21 with MBD6$^{C\Delta+StkyC}$ in wild-type or *acd15 acd21* double mutant plants (Fig. 4H). ACD21 showed a reduced correlation with MBD6$^{C\Delta+StkyC}$ in *acd15 acd21* plants compared to wild type (0.48 vs 0.79), a reduction of colocalization with MBD6 across nuclei, and a visible increase in ACD21 cytosolic localization, suggesting that ACD21 requires ACD15

235 to associate properly with MBD6$^{C\Delta+StkyC}$ (Fig.4I and S4H-I). On the other hand, ACD15
236 correlated strongly with MBD6$^{C\Delta+StkyC}$ in *acd15 acd21* plants (r = 0.92), maintained strong
237 nuclear signal, and directly overlapped with nuclear MBD6, demonstrating that ACD15 does not
238 require ACD21 for proper localization with MBD6$^{C\Delta+StkyC}$ (Fig. 4H and S4J). These experiments
239 demonstrate that the StkyC domain of MBD6 is required for the function of the MBD5/6
240 complex, is needed for proper localization of ACD15 and ACD21, and mediates the
241 accumulation of MBD6 at heterochromatic foci through ACD15 and ACD21.
242
243 **ACD15 and ACD21 can mediate functional and targeted gene silencing foci.**
244 Some ACD containing sHSP proteins are known to form dynamic oligomeric assemblies as part
245 of their function in maintaining protein homeostasis (*16*), which could explain how
246 ACD15/ACD21 drive high levels of MBD5/6 complex accumulation at meCG dense
247 heterochromatin. To further explore this concept, we created a system to target MBD5/6
248 complexes to a discrete genomic location outside of pericentromeric heterochromatin. We
249 utilized the SunTag system(*38*), composed of a dead Cas9 protein (dCas9) fused to ten single-
250 chain variable fragment (scFv) binding sites, targeted to the promoter of the euchromatic *FWA*
251 gene (*39*). To nucleate MBD5/6 foci at the dCas9 binding site we fused the scFv to the StkyC
252 domain of MBD6 and to GFP, to visualize the nuclear distribution of the fusion proteins (Fig.
253 5A).
254 If ACD15 and ACD21 drive higher order multimerization of MBD5/6 complexes, we
255 would expect to observe discrete GFP foci in nuclei representing the dCas9 binding sites, as well
256 as other foci corresponding to chromocenters since the scFv-GFP-StykC fusion would likely be
257 recruited into multimerized MBD5/6 complexes at heterochromatin sites (Fig. 5A). Indeed, we
258 observed an average of 6.4 GFP foci per nucleus in SunTag^{StkyC} expressing wild-type plants (Fig.
259 5B, C), some of which overlapped with DAPI staining chromocenters and others that did not
260 (fig. S5A). We also transformed SunTag^{StkyC} into the *mbd5 mbd6* mutant, which would be
261 predicted to eliminate recruitment of the scFv-GFP-StykC fusion protein into chromocenters by
262 elimination of meCG bound endogenous MBD5/6 complexes. As predicted, we now observed
263 an average of only two foci per nucleus (Fig. 5B, C), likely corresponding to the *FWA* alleles on
264 the two homologous chromosomes. Consistent with these foci representing dCas9 bound to
265 euchromatic *FWA* (*39*), these foci did not overlap with DAPI staining chromocenters (fig. S5B).
266 Notably, the volume of SunTag^{StkyC} foci were increased in *mbd5 mbd6* (Fig. 5D), with the vast
267 majority of nuclear GFP signal accumulating at the two nuclear bodies (Fig. 5B), suggesting that
268 excess scFv-GFP-StykC fusion protein shifted from heterochromatic regions to the dCas9
269 binding sites.
270 We also expressed the SunTag^{StkyC} system in *acd15 acd21* mutants to determine if
271 ACD15 and ACD21 are required for foci formation. Indeed, SunTag^{StkyC} now only displayed
272 diffuse nucleoplasmic GFP signal, lacking detectable foci (Fig. 5B, C). This pattern was similar
273 to control plants expressing a SunTag-TET1 system(*40*), in which the scFv was fused to GFP
274 and the human TET1 protein, suggesting that the GFP foci observed in SunTag^{StkyC} is not a
275 general property or artifact of the SunTag system (fig. S5C). We also introduced the SunTag^{StkyC}
276 system into the *sln* genetic background and observed GFP foci counts and localization similar to
277 the wild-type plants, showing around 6.1 foci per nucleus (Fig. 5B,C). These results demonstrate
278 that ACD15/21 are necessary and sufficient to drive high level accumulation of MBD5/6
279 complexes at discrete foci.
280 We next tested if the foci formed by the SunTag^{StkyC} system are capable of gene
281 silencing. The *FWA* gene is normally methylated and silent in wild-type plants. However, stably
282 unmethylated and expressed *fwa* epigenetic alleles exist that cause a later flowering phenotype

(*41*, *42*). This allowed us to test if the SunTag^{StkyC} system could silence *FWA* by introducing the system into the *fwa* epigenetic background. Indeed, we found a significant suppression of *FWA* expression compared to *fwa* control plants (Fig. 5E). *fwa* plants expressing SunTag^{StkyC} also flowered earlier on average, showing a decrease in the number of leaves produced before flowering compared to *fwa* mutant plants (Fig. 5F-G). Correlation of *fwa* expression with leaf counts for *fwa* SunTag^{StkyC} plants showed a strong positive correlation as expected (fig. S5D).

Lastly, we tested whether the SunTag^{StkyC} system could complement the *FWA* derepression phenotype of MBD5/6 complex mutants (Fig. 1E)(*29*). Interestingly, SunTag^{StkyC} was able to silence *FWA* in *mbd5 mbd6* mutant plants demonstrating that the tethering function of MBD6 could be largely replaced by targeting with the StkyC domain, and that silencing can occur without the methyl binding proteins (fig. S5E). Surprisingly, SunTag^{StkyC} could also partially complement *FWA* derepression in the *sln* mutant background, while SunTag^{StkyC} could not complement *FWA* derepression in the *acd15 acd21* mutant background (fig. S5F,G). These results demonstrate that the SunTag^{StkyC} system maintains some gene silencing capability without SLN, suggesting that ACD15 and ACD21 alone possess silencing ability.

Concluding remarks

Our results provide evidence for distinct mechanistic roles for ACD15, ACD21, and SLN in the formation and regulation of the meCG specific MBD5/6 silencing complex (fig. S6). ACD15 and ACD21 function to both drive the formation of higher order MBD5/6 complex assemblies, and bridge SLN to the complex. In contrast, the main role of SLN appears to be regulation of the dynamics of protein mobility within these complex assemblies. The activity of both ACD15/21 and SLN are clearly required for proper silencing function of the complex. The accumulation of multiple MBD5/6 proteins into higher order complex assemblies can explain why these complexes preferentially localize to high density meCG sites in the genome, likely via cooperative binding to closely spaced meCG sites.

ACD domain containing small HSPs are found in all eukaryotic lineages and are most well known for their role in regulating the aggregation of proteins (*14*, *15*, *17*, *34*, *43*). In the MBD5/6 complex however, the oligomerization capacities of ACD15 and ACD21 are specifically co-opted to control complex multimerization and silencing function. It seems likely that ACD proteins in other systems may also play important roles outside of general protein homeostasis.

316 **References and Notes**

317 1. S. F. Banani, H. O. Lee, A. A. Hyman, M. K. Rosen, Biomolecular condensates: organizers
318 of cellular biochemistry. *Nat Rev Mol Cell Biol*. **18**, 285–298 (2017).

319 2. A. A. Hyman, C. A. Weber, F. Jülicher, Liquid-Liquid Phase Separation in Biology. *Annual*
320 *Review of Cell and Developmental Biology*. **30**, 39–58 (2014).

321 3. Y. Shin, C. P. Brangwynne, Liquid phase condensation in cell physiology and disease.
322 *Science*. **357** (2017), doi:10.1126/science.aaf4382.

323 4. M. Feric, N. Vaidya, T. S. Harmon, D. M. Mitrea, L. Zhu, T. M. Richardson, R. W. Kriwacki,
324 R. V. Pappu, C. P. Brangwynne, Coexisting Liquid Phases Underlie Nucleolar
325 Subcompartments. *Cell*. **165**, 1686–1697 (2016).

326 5. D. L. J. Lafontaine, J. A. Riback, R. Bascetin, C. P. Brangwynne, The nucleolus as a
327 multiphase liquid condensate. *Nat Rev Mol Cell Biol*. **22**, 165–182 (2021).

328 6. A. Boija, I. A. Klein, B. R. Sabari, A. Dall'Agnese, E. L. Coffey, A. V. Zamudio, C. H. Li,
329 K. Shrinivas, J. C. Manteiga, N. M. Hannett, B. J. Abraham, L. K. Afeyan, Y. E. Guo, J. K.
330 Rimel, C. B. Fant, J. Schuijers, T. I. Lee, D. J. Taatjes, R. A. Young, Transcription Factors
331 Activate Genes through the Phase-Separation Capacity of Their Activation Domains. *Cell*.
332 **175**, 1842-1855.e16 (2018).

333 7. J. E. Henninger, O. Oksuz, K. Shrinivas, I. Sagi, G. LeRoy, M. M. Zheng, J. O. Andrews, A.
334 V. Zamudio, C. Lazaris, N. M. Hannett, T. I. Lee, P. A. Sharp, I. I. Cissé, A. K. Chakraborty,
335 R. A. Young, RNA-Mediated Feedback Control of Transcriptional Condensates. *Cell*. **184**,
336 207-225.e24 (2021).

337 8. A. Zbinden, M. Pérez-Berlanga, P. De Rossi, M. Polymenidou, Phase Separation and
338 Neurodegenerative Diseases: A Disturbance in the Force. *Developmental Cell*. **55**, 45–68
339 (2020).

340 9. M. A. Mensah, H. Niskanen, A. P. Magalhaes, S. Basu, M. Kircher, H. L. Sczakiel, A. M. V.
341 Reiter, J. Elsner, P. Meinecke, S. Biskup, B. H. Y. Chung, G. Dombrowsky, C. Eckmann-
342 Scholz, M. P. Hitz, A. Hoischen, P.-M. Holterhus, W. Hülsemann, K. Kahrizi, V. M.
343 Kalscheuer, A. Kan, M. Krumbiegel, I. Kurth, J. Leubner, A. C. Longardt, J. D. Moritz, H.
344 Najmabadi, K. Skipalova, L. Snijders Blok, A. Tzschach, E. Wiedersberg, M. Zenker, C.
345 Garcia-Cabau, R. Buschow, X. Salvatella, M. L. Kraushar, S. Mundlos, A. Caliebe, M.
346 Spielmann, D. Horn, D. Hnisz, Aberrant phase separation and nucleolar dysfunction in rare
347 genetic diseases. *Nature*. **614**, 564–571 (2023).

348 10. M. H. Al-Whaibi, Plant heat-shock proteins: A mini review. *Journal of King Saud University*
349 *- Science*. **23**, 139–150 (2011).

350 11. F. Hennessy, W. S. Nicoll, R. Zimmermann, M. E. Cheetham, G. L. Blatch, Not all J domains
351 are created equal: Implications for the specificity of Hsp40–Hsp70 interactions. *Protein Sci*.
352 **14**, 1697–1709 (2005).

12. R. Imamoglu, D. Balchin, M. Hayer-Hartl, F. U. Hartl, Bacterial Hsp70 resolves misfolded states and accelerates productive folding of a multi-domain protein. *Nature Communications*. **11**, 365 (2020).

13. H. H. Kampinga, C. Andreasson, A. Barducci, M. E. Cheetham, D. Cyr, C. Emanuelsson, P. Genevaux, J. E. Gestwicki, P. Goloubinoff, J. Huerta-Cepas, J. Kirstein, K. Liberek, M. P. Mayer, K. Nagata, N. B. Nillegoda, P. Pulido, C. Ramos, P. De los Rios, S. Rospert, R. Rosenzweig, C. Sahi, M. Taipale, B. Tomiczek, R. Ushioda, J. C. Young, R. Zimmermann, A. Zylicz, M. Zylicz, E. A. Craig, J. Marszalek, Function, evolution, and structure of J-domain proteins. *Cell Stress and Chaperones*. **24**, 7–15 (2019).

14. M. Haslbeck, S. Weinkauf, J. Buchner, Small heat shock proteins: Simplicity meets complexity. *J Biol Chem*. **294**, 2121–2132 (2019).

15. J. M. Webster, A. L. Darling, V. N. Uversky, L. J. Blair, Small Heat Shock Proteins, Big Impact on Protein Aggregation in Neurodegenerative Disease. *Front Pharmacol*. **10** (2019), doi:10.3389/fphar.2019.01047.

16. M. Haslbeck, E. Vierling, A First Line of Stress Defense: Small Heat Shock Proteins and Their Function in Protein Homeostasis. *Journal of Molecular Biology*. **427**, 1537–1548 (2015).

17. W. C. Boelens, Structural aspects of the human small heat shock proteins related to their functional activities. *Cell Stress and Chaperones*. **25**, 581–591 (2020).

18. H. Yoo, J. A. M. Bard, E. Pilipenko, D. A. Drummond, "Chaperones directly and efficiently disperse stress-triggered biomolecular condensates" (2021), p. 2021.05.13.444070, , doi:10.1101/2021.05.13.444070.

19. H. Yu, S. Lu, K. Gasior, D. Singh, S. Vazquez-Sanchez, O. Tapia, D. Toprani, M. S. Beccari, J. R. Yates, S. D. Cruz, J. M. Newby, M. Lafarga, A. S. Gladfelter, E. Villa, D. W. Cleveland, HSP70 chaperones RNA-free TDP-43 into anisotropic intranuclear liquid spherical shells. *Science* (2020), doi:10.1126/science.abb4309.

20. Z. Liu, S. Zhang, J. Gu, Y. Tong, Y. Li, X. Gui, H. Long, C. Wang, C. Zhao, J. Lu, L. He, Y. Li, Z. Liu, D. Li, C. Liu, Hsp27 chaperones FUS phase separation under the modulation of stress-induced phosphorylation. *Nat Struct Mol Biol*. **27**, 363–372 (2020).

21. E. W. J. Wallace, J. L. Kear-Scott, E. V. Pilipenko, M. H. Schwartz, P. R. Laskowski, A. E. Rojek, C. D. Katanski, J. A. Riback, M. F. Dion, A. M. Franks, E. M. Airoldi, T. Pan, B. A. Budnik, D. A. Drummond, Reversible, Specific, Active Aggregates of Endogenous Proteins Assemble upon Heat Stress. *Cell*. **162**, 1286–1298 (2015).

22. E. Chytilova, J. Macas, E. Sliwinska, S. M. Rafelski, G. M. Lambert, D. W. Galbraith, Nuclear Dynamics in Arabidopsis thaliana. *Mol Biol Cell*. **11**, 2733–2741 (2000).

23. R. J. Emenecker, A. S. Holehouse, L. C. Strader, *Annual Review of Plant Biology*, in press, doi:10.1146/annurev-arplant-081720-015238.

24. S. Zhao, L. Cheng, Y. Gao, B. Zhang, X. Zheng, L. Wang, P. Li, Q. Sun, H. Li, Plant HP1 protein ADCP1 links multivalent H3K9 methylation readout to heterochromatin formation. *Cell Res*. **29**, 54–66 (2019).

25. G. Grafi, A. Zemach, L. Pitto, Methyl-CpG-binding domain (MBD) proteins in plants. *Biochim. Biophys. Acta*. **1769**, 287–294 (2007).

26. S. Feng, Z. Zhong, M. Wang, S. E. Jacobsen, Efficient and accurate determination of genome-wide DNA methylation patterns in Arabidopsis thaliana with enzymatic methyl sequencing. *Epigenetics & Chromatin*. **13**, 42 (2020).

27. C. J. Harris, M. Scheibe, S. P. Wongpalee, W. Liu, E. M. Cornett, R. M. Vaughan, X. Li, W. Chen, Y. Xue, Z. Zhong, L. Yen, W. D. Barshop, S. Rayatpisheh, J. Gallego-Bartolome, M. Groth, Z. Wang, J. A. Wohlschlegel, J. Du, S. B. Rothbart, F. Butter, S. E. Jacobsen, A DNA methylation reader complex that enhances gene transcription. *Science*. **362**, 1182–1186 (2018).

28. Z. Lang, M. Lei, X. Wang, K. Tang, D. Miki, H. Zhang, S. K. Mangrauthia, W. Liu, W. Nie, G. Ma, J. Yan, C.-G. Duan, C.-C. Hsu, C. Wang, W. A. Tao, Z. Gong, J.-K. Zhu, The Methyl-CpG-Binding Protein MBD7 Facilitates Active DNA Demethylation to Limit DNA Hyper-Methylation and Transcriptional Gene Silencing. *Molecular Cell*. **57**, 971–983 (2015).

29. L. Ichino, B. A. Boone, L. Strauskulage, C. J. Harris, G. Kaur, M. A. Gladstone, M. Tan, S. Feng, Y. Jami-Alahmadi, S. H. Duttke, J. A. Wohlschlegel, X. Cheng, S. Redding, S. E. Jacobsen, MBD5 and MBD6 couple DNA methylation to gene silencing through the J-domain protein SILENZIO. *Science* (2021), doi:10.1126/science.abg6130.

30. D. Li, A. M. S. Palanca, S. Y. Won, L. Gao, Y. Feng, A. A. Vashisht, L. Liu, Y. Zhao, X. Liu, X. Wu, S. Li, B. Le, Y. J. Kim, G. Yang, S. Li, J. Liu, J. A. Wohlschlegel, H. Guo, B. Mo, X. Chen, J. A. Law, The MBD7 complex promotes expression of methylated transgenes without significantly altering their methylation status. *eLife*. **6**, e19893 (2017).

31. Z. Feng, X. Zhan, J. Pang, X. Liu, H. Zhang, Z. Lang, J.-K. Zhu, Genetic analysis implicates a molecular chaperone complex in regulating epigenetic silencing of methylated genomic regions. *Journal of Integrative Plant Biology*. **63**, 1451–1461 (2021).

32. J. Jumper, R. Evans, A. Pritzel, T. Green, M. Figurnov, O. Ronneberger, K. Tunyasuvunakool, R. Bates, A. Žídek, A. Potapenko, A. Bridgland, C. Meyer, S. A. A. Kohl, A. J. Ballard, A. Cowie, B. Romera-Paredes, S. Nikolov, R. Jain, J. Adler, T. Back, S. Petersen, D. Reiman, E. Clancy, M. Zielinski, M. Steinegger, M. Pacholska, T. Berghammer, S. Bodenstein, D. Silver, O. Vinyals, A. W. Senior, K. Kavukcuoglu, P. Kohli, D. Hassabis, Highly accurate protein structure prediction with AlphaFold. *Nature*. **596**, 583–589 (2021).

33. R. Evans, M. O'Neill, A. Pritzel, N. Antropova, A. Senior, T. Green, A. Žídek, R. Bates, S. Blackwell, J. Yim, O. Ronneberger, S. Bodenstein, M. Zielinski, A. Bridgland, A. Potapenko, A. Cowie, K. Tunyasuvunakool, R. Jain, E. Clancy, P. Kohli, J. Jumper, D. Hassabis, Protein complex prediction with AlphaFold-Multimer (2022), p. 2021.10.04.463034, , doi:10.1101/2021.10.04.463034.

429 34. G. K. A. Hochberg, D. A. Shepherd, E. G. Marklund, I. Santhanagoplan, M. T. Degiacomi,
430 A. Laganowsky, T. M. Allison, E. Basha, M. T. Marty, M. R. Galpin, W. B. Struwe, A. J.
431 Baldwin, E. Vierling, J. L. P. Benesch, Structural principles that enable oligomeric small
432 heat-shock protein paralogs to evolve distinct functions. *Science*. **359**, 930–935 (2018).

433 35. R. Rosenzweig, N. B. Nillegoda, M. P. Mayer, B. Bukau, The Hsp70 chaperone network.
434 *Nature Reviews Molecular Cell Biology*. **20**, 665–680 (2019).

435 36. A. Zemach, Y. Li, B. Wayburn, H. Ben-Meir, V. Kiss, Y. Avivi, V. Kalchenko, S. E.
436 Jacobsen, G. Grafi, DDM1 binds Arabidopsis methyl-CpG binding domain proteins and
437 affects their subnuclear localization. *Plant Cell*. **17**, 1549–1558 (2005).

438 37. N. N. Giakoumakis, M. A. Rapsomaniki, Z. Lygerou, Analysis of Protein Kinetics Using
439 Fluorescence Recovery After Photobleaching (FRAP). *Methods Mol. Biol.* **1563**, 243–267
440 (2017).

441 38. J. Gardiner, B. Ghoshal, M. Wang, S. E. Jacobsen, CRISPR–Cas-mediated transcriptional
442 control and epi-mutagenesis. *Plant Physiology*. **188**, 1811–1824 (2022).

443 39. W. J. J. Soppe, Z. Jasencakova, A. Houben, T. Kakutani, A. Meister, M. S. Huang, S. E.
444 Jacobsen, I. Schubert, P. F. Fransz, DNA methylation controls histone H3 lysine 9
445 methylation and heterochromatin assembly in Arabidopsis. *The EMBO Journal*. **21**, 6549–
446 6559 (2002).

447 40. B. Ghoshal, B. Vong, C. L. Picard, S. Feng, J. M. Tam, S. E. Jacobsen, A viral guide RNA
448 delivery system for CRISPR-based transcriptional activation and heritable targeted DNA
449 demethylation in Arabidopsis thaliana. *PLOS Genetics*. **16**, e1008983 (2020).

450 41. J. Gallego-Bartolomé, W. Liu, P. H. Kuo, S. Feng, B. Ghoshal, J. Gardiner, J. M.-C. Zhao,
451 S. Y. Park, J. Chory, S. E. Jacobsen, Co-targeting RNA Polymerases IV and V Promotes
452 Efficient De Novo DNA Methylation in Arabidopsis. *Cell*. **176**, 1068-1082.e19 (2019).

453 42. M. Wang, Z. Zhong, J. Gallego-Bartolomé, Z. Li, S. Feng, H. Y. Kuo, R. L. Kan, H. Lam, J.
454 C. Richey, L. Tang, J. Zhou, M. Liu, Y. Jami-Alahmadi, J. Wohlschlegel, S. E. Jacobsen, A
455 gene silencing screen uncovers diverse tools for targeted gene repression in Arabidopsis. *Nat.*
456 *Plants*. **9**, 460–472 (2023).

457 43. E. R. Waters, E. Vierling, Plant small heat shock proteins – evolutionary and functional
458 diversity. *New Phytologist*. **227**, 24–37 (2020).

459 44. L. Yan, S. Wei, Y. Wu, R. Hu, H. Li, W. Yang, Q. Xie, High-Efficiency Genome Editing in
460 Arabidopsis Using YAO Promoter-Driven CRISPR/Cas9 System. *Molecular Plant*. **8**, 1820–
461 1823 (2015).
462
463 45. C. Zhao, D. J. Segal, S. E. Jacobsen, Targeted DNA demethylation of the Arabidopsis
464 genome using the human TET1 catalytic domain. *Proceedings of the National Academy*
465 *of Sciences*. **115**, E2125–E2134 (2018).
466
467

46. B. Ghoshal, J. Gardiner, "CRISPR-dCas9-Based Targeted Manipulation of DNA Methylation in Plants" in *CRISPR-Cas Methods: Volume 2*, M. T. Islam, K. A. Molla, Eds. (Springer US, New York, NY, 2021; https://doi.org/10.1007/978-1-0716-1657-4_5), *Springer Protocols Handbooks*, pp. 57–71.

47. C. S. Hughes, S. Foehr, D. A. Garfield, E. E. Furlong, L. M. Steinmetz, J. Krijgsveld, Ultrasensitive proteome analysis using paramagnetic bead technology. *Molecular Systems Biology*. **10**, 757 (2014).

48. J. Cox, M. Mann, MaxQuant enables high peptide identification rates, individualized p.p.b.-range mass accuracies and proteome-wide protein quantification. *Nat Biotechnol*. **26**, 1367–1372 (2008).

49. B. Langmead, S. L. Salzberg, Fast gapped-read alignment with Bowtie 2. *Nat Methods*. **9**, 357–359 (2012).

50. F. Ramírez, D. P. Ryan, B. Grüning, V. Bhardwaj, F. Kilpert, A. S. Richter, S. Heyne, F. Dündar, T. Manke, deepTools2: a next generation web server for deep-sequencing data analysis. *Nucleic Acids Research*. **44**, W160–W165 (2016).

51. Y. Zhang, T. Liu, C. A. Meyer, J. Eeckhoute, D. S. Johnson, B. E. Bernstein, C. Nusbaum, R. M. Myers, M. Brown, W. Li, X. S. Liu, Model-based analysis of ChIP-Seq (MACS). *Genome Biol*. **9**, R137 (2008).

52. S. Heinz, C. Benner, N. Spann, E. Bertolino, Y. C. Lin, P. Laslo, J. X. Cheng, C. Murre, H. Singh, C. K. Glass, Simple combinations of lineage-determining transcription factors prime cis-regulatory elements required for macrophage and B cell identities. *Mol Cell*. **38**, 576–589 (2010).

53. L. Ichino, C. L. Picard, J. Yun, M. Chotai, S. Wang, E. K. Lin, R. K. Papareddy, Y. Xue, S. E. Jacobsen, Single-nucleus RNA-seq reveals that MBD5, MBD6, and SILENZIO maintain silencing in the vegetative cell of developing pollen. *Cell Reports*. **41**, 111699 (2022).

54. A. Dobin, C. A. Davis, F. Schlesinger, J. Drenkow, C. Zaleski, S. Jha, P. Batut, M. Chaisson, T. R. Gingeras, STAR: ultrafast universal RNA-seq aligner. *Bioinformatics*. **29**, 15–21 (2013).

55. S. Anders, P. T. Pyl, W. Huber, HTSeq—a Python framework to work with high-throughput sequencing data. *Bioinformatics*. **31**, 166–169 (2015).

56. M. I. Love, W. Huber, S. Anders, Moderated estimation of fold change and dispersion for RNA-seq data with DESeq2. *Genome Biology*. **15**, 550 (2014).

57. A. R. Quinlan, I. M. Hall, BEDTools: a flexible suite of utilities for comparing genomic features. *Bioinformatics*. **26**, 841–842 (2010).

Acknowledgments: We thank Suhua Feng, Mahnaz Akhavan and the Broad Stem Cell Research Center Biosequencing core for DNA sequencing, and Julie Law for *lil-1* mutant seeds.

Funding:
National Institutes of Health grant R35 GM130272 (SEJ), R01 GM089778 (JAW)
The Philip Whitcome Pre-Doctoral Fellowship in Molecular Biology to B.A.B and to L.I.
SEJ is an Investigator of the Howard Hughes Medical Institute

Author contributions:
Conceptualization: BAB, LI, SEJ
Investigation: BAB, LI, SW, JY, YJA, JS, CM, BS, AVA, SKL, IT
Resources: SEJ
Software: BAB, LI, SW
Validation: BAB, LI, SW
Data curation: BAB, LI
Formal Analysis: BAB, LI, SW
Funding acquisition: BAB, LI, SEJ
Methodology: BAB
Visualization: BAB, LI, SW
Project administration: BAB, SEJ
Supervision: JAW, SEJ
Writing – original draft: BAB, LI, SEJ
Writing – review & editing: BAB, LI, SEJ

Competing interests: Authors declare that they have no competing interests.

Data and materials availability:
The high-throughput sequencing data generated in this paper have been deposited in the Gene Expression Omnibus (GEO) database (accession no. TBD).

Supplementary Materials
Materials and Methods
Supplementary Text
Figs. S1 to S6
Table S1
References (*1–57*)

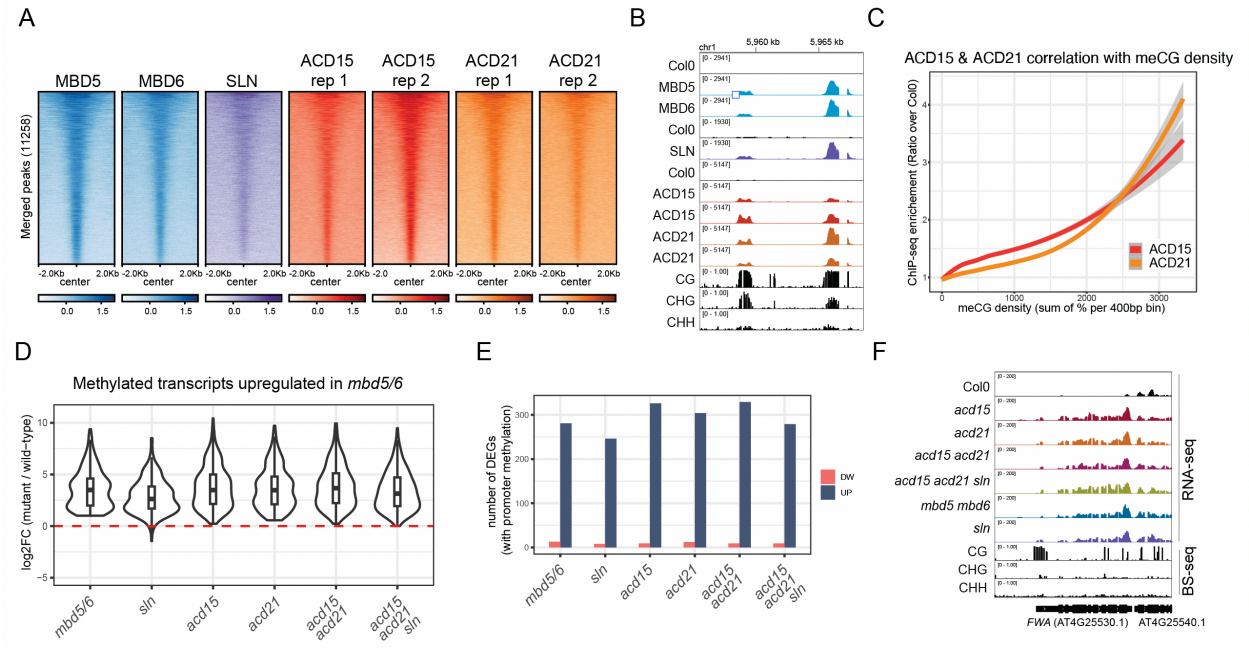

Fig. 1. ACD15 and ACD21 are required for silencing.
(A) Heatmap of FLAG-tagged MBD5, MBD6, SLN, ACD15, and ACD21 ChIP-seq enrichment (log2FC over no-FLAG Col0 control) centered at all merged peaks. **(B)** Genome browser image of ChIP-seq data showing two methylated loci co-bound by all MBD5/6 complex members. **(C)** Loess curves showing correlation between ChIP-seq enrichment for a representative replicate and CG methylation density. **(D)** Violin plots showing mature pollen RNA-seq data for the indicated mutants, at *mbd5 mbd6* upregulated transcripts (6 replicates per genotype). **(E)** Comparison between genotypes of the number of RNA-seq differentially expressed genes (DEGs) with >40% CG methylation levels around the TSS. **(F)** Genome browser image of RNA-seq data at the *FWA* locus in the indicated genotypes. Wild-type BS-seq data is shown as reference.

A

	BAIT ->	none	MBD5-FLAG		MBD6-FLAG		none		SLN-FLAG				none		ACD15-FLAG			ACD21-FLAG			none		SLN-FLAG			none	MBD5-FLAG		MBD6-FLAG	
	genetic background ->	Col0	Col0	*sln*	Col0	*sln*	Col0	Col0	Col0	Col0	*mbd5/6*	*mbd5/6*	Col0	Col0	Col0	*acd15 acd21*	*sln*	Col0	*acd15 acd21*	*sln*	Col0	Col0	*sln*	*acd21*	*acd15 acd21*	Col0	Col0	*acd15 acd21*	Col0	*acd15 acd21*
MBD5	AT3G46580.1	1	151	143	73	59	0	0	112	119	0	0	0	3	159	85	123	171	0	153	0	0	80	0	0	5	165	91	70	0
MBD6	AT5G59380.1	1	103	111	168	150	0	0	136	124	0	1	0	0	160	87	125	164	0	164	0	0	84	0	0	5	84	0	345	127
ACD15	AT1G76440.3	2	81	74	58	50	0	0	56	58	12	13	0	0	94	67	84	63	0	81	0	0	37	1	0	3	52	3	78	0
ACD21	AT1G54850.1	0	194	134	115	118	0	0	140	113	7	8	0	2	254	0	186	290	116	243	1	0	102	0	0	3	178	0	269	2
SLN	AT5G37380.9	0	46	0	69	0	0	0	201	144	87	99	0	0	87	0	0	84	1	0	0	0	134	37	69	0	80	0	122	0

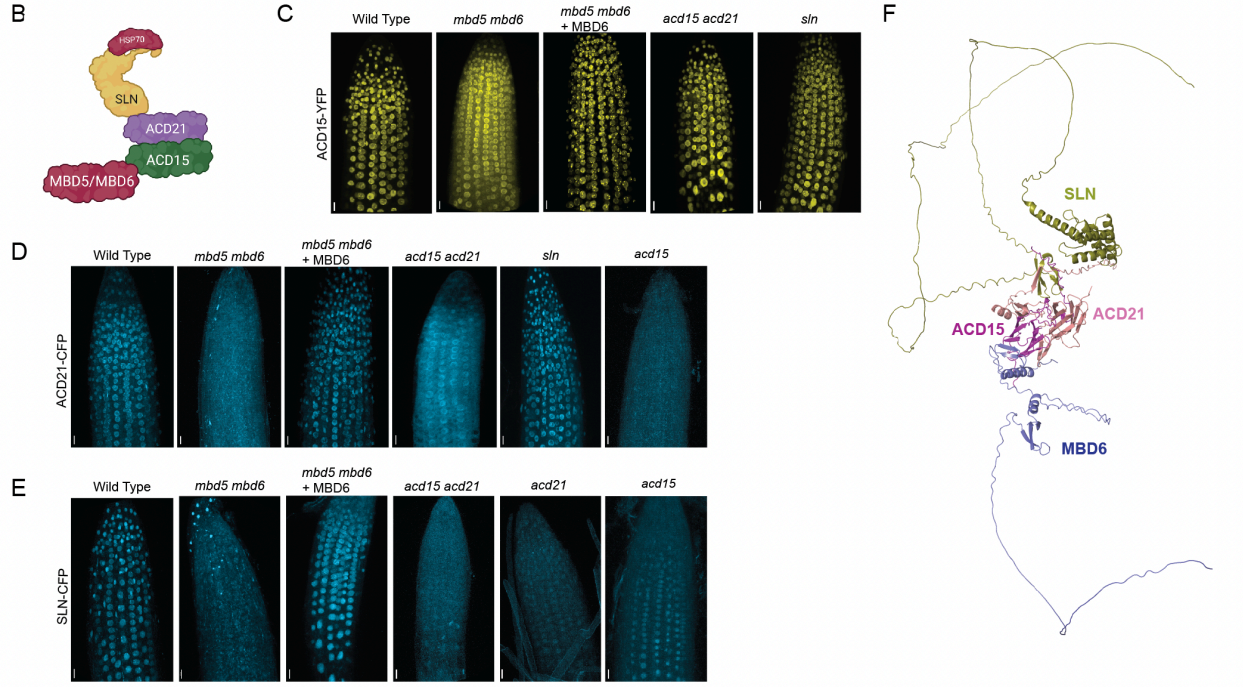

Fig. 2. ACD15 and ACD21 bridge SLN to MBD5/6.
(A) IP-MS of flag-tagged MBD5/6 complex members in the indicated genetic backgrounds (MS/MS counts). **(B)** MBD5/6 complex organization as predicted by IP-MS. Created with BioRender.com (**C-E)** 3D reconstruction of root meristems of plants expressing fluorescently tagged ACD15, ACD21, or SLN in wild-type (Col0) and mutant backgrounds. Scale bar = 20 µm. **(F)** Predicted structure of MBD5/6 complex from AlphaFold Multimer (*33*). MBD6=Blue, ACD15=magenta, ACD21=maroon, SLN=gold.

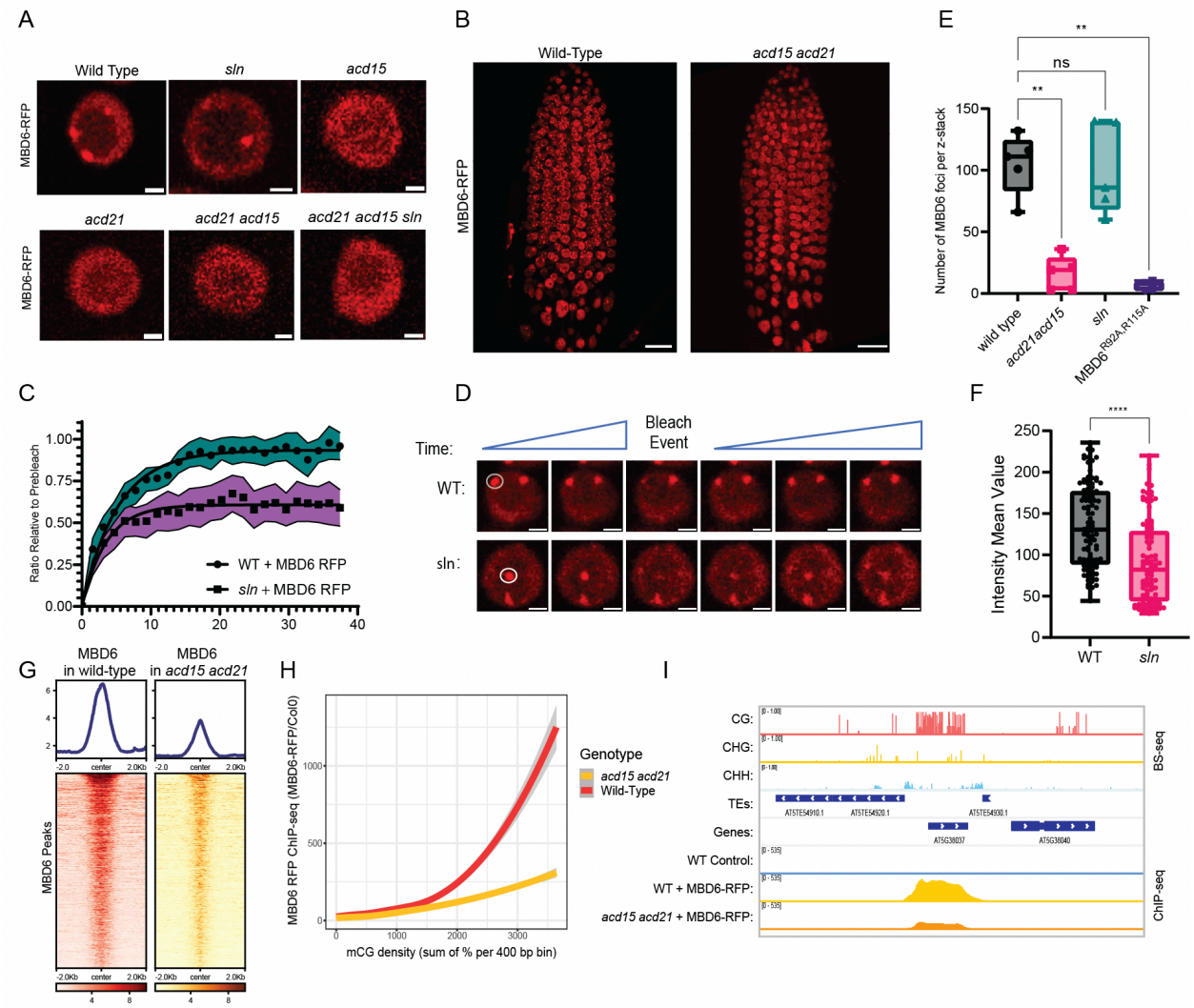

Fig. 3. ACD15, ACD21, and SLN regulate MBD6 accumulation and mobility.
(A) Representative MBD6-RFP nuclear images in mutant backgrounds. Scale bar = 2µM. **(B)** 3D reconstruction of MBD6-RFP root meristem z-stacks. Scale bar = 20µM. **(C)** FRAP recovery curves comparing MBD6 signal in WT and *sln* plants. Shaded area: 95% confidence interval of FRAP data (N=25 from 5 plants lines), dots: mean values, line: fitted one-phase, non-linear regression. **(D)** Representative image of FRAP experiment. White circles indicate foci chosen for bleaching. Scale bars = 2µM **(E)** MBD6 foci counts across 50 slice Z-stacks of root meristems from five plant lines per genotype. Welch's ANOVA and Dunnet's T3 multiple comparisons test (**: P<0.01, NS: P>=0.05). **(F)** Box plots of mean intensity values of MBD6 foci (5 individual plants per genotype). Two-tailed t-test (****: P<0.0001). **(G)** Heatmaps and metaplots of MBD6-RFP ChIP-seq signal (log2 ratio over no-FLAG Col0 control) at peaks called in "MBD6-RFP in wild-type" dataset. **(H)** Loess curves showing correlation between MBD6-RFP ChIP-seq enrichment and CG methylation density. **(I)** Genome browser tracks showing an example of a high density meCG site bound by MBD6-RFP (ChIP-Seq). Wild-type BS-seq data is shown as reference.

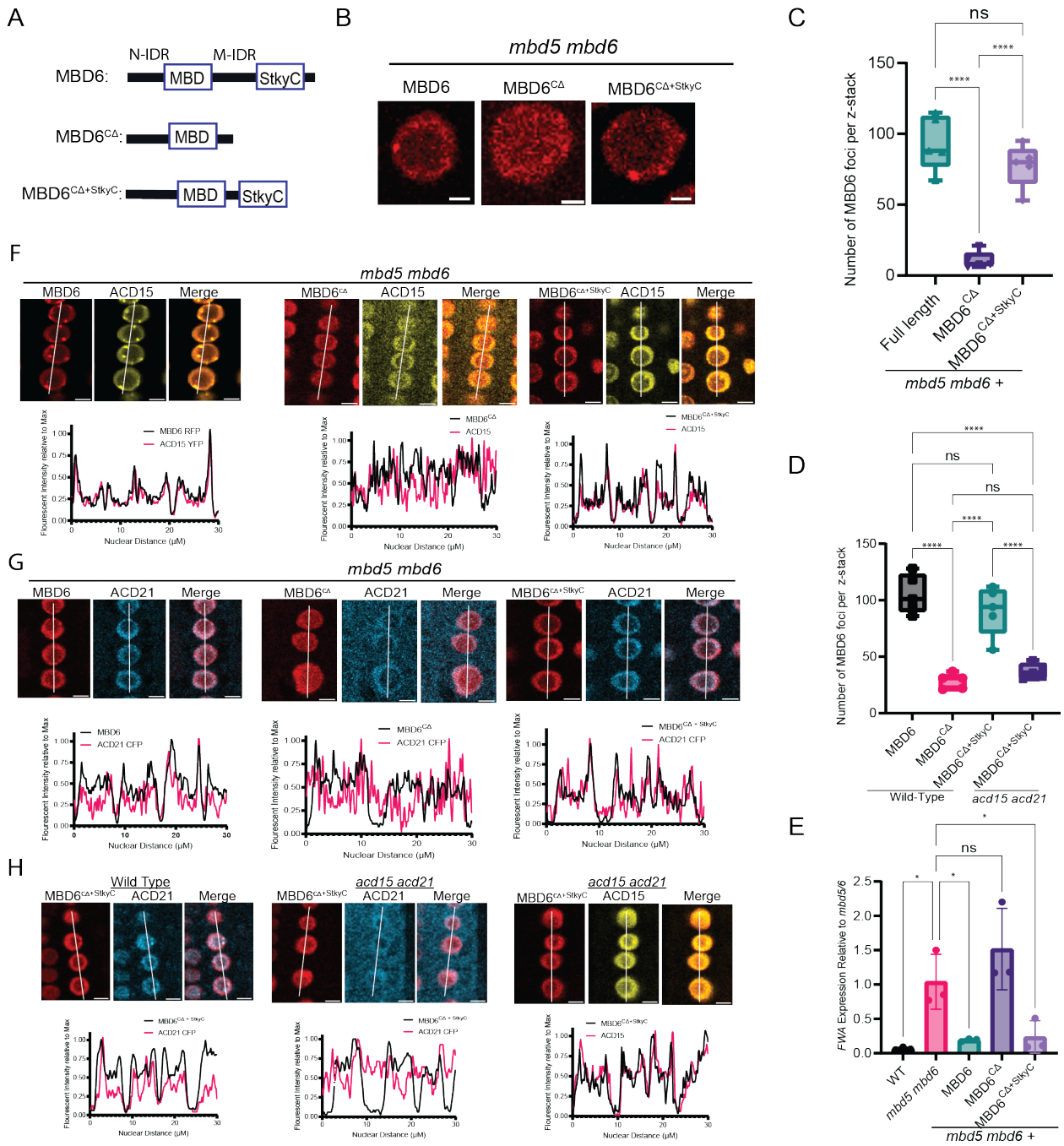

Fig. 4. StkyC domain of MBD6 is necessary for function and localization of MBD6. **(A)** Graphical description of MBD6 mutant constructs. **(B)** Representative nuclei showing MBD6-RFP signal. Scale bar = 2 µM. **(C-D)** Number of MBD6 nuclear foci (5 different plants lines per sample, Z-stack of 50 slices). Brown-Forsythe ANOVA with Tukey's multiple corrections test (****: P<0.0001, NS: P>=0.05). **(E)** *FWA* expression from RT-qPCR of flower bud RNA. Brown-Forsythe ANOVA with Dunnet's multiple corrections test (*: P<0.05, NS: P>=0.05). **(F-H)** Representative images and nuclear profile plots of MBD6-RFP mutants with either ACD15-YFP or ACD21-CFP. White lines indicate the region plotted in the graphs ("nuclear distance"). Scale bars = 10µM.

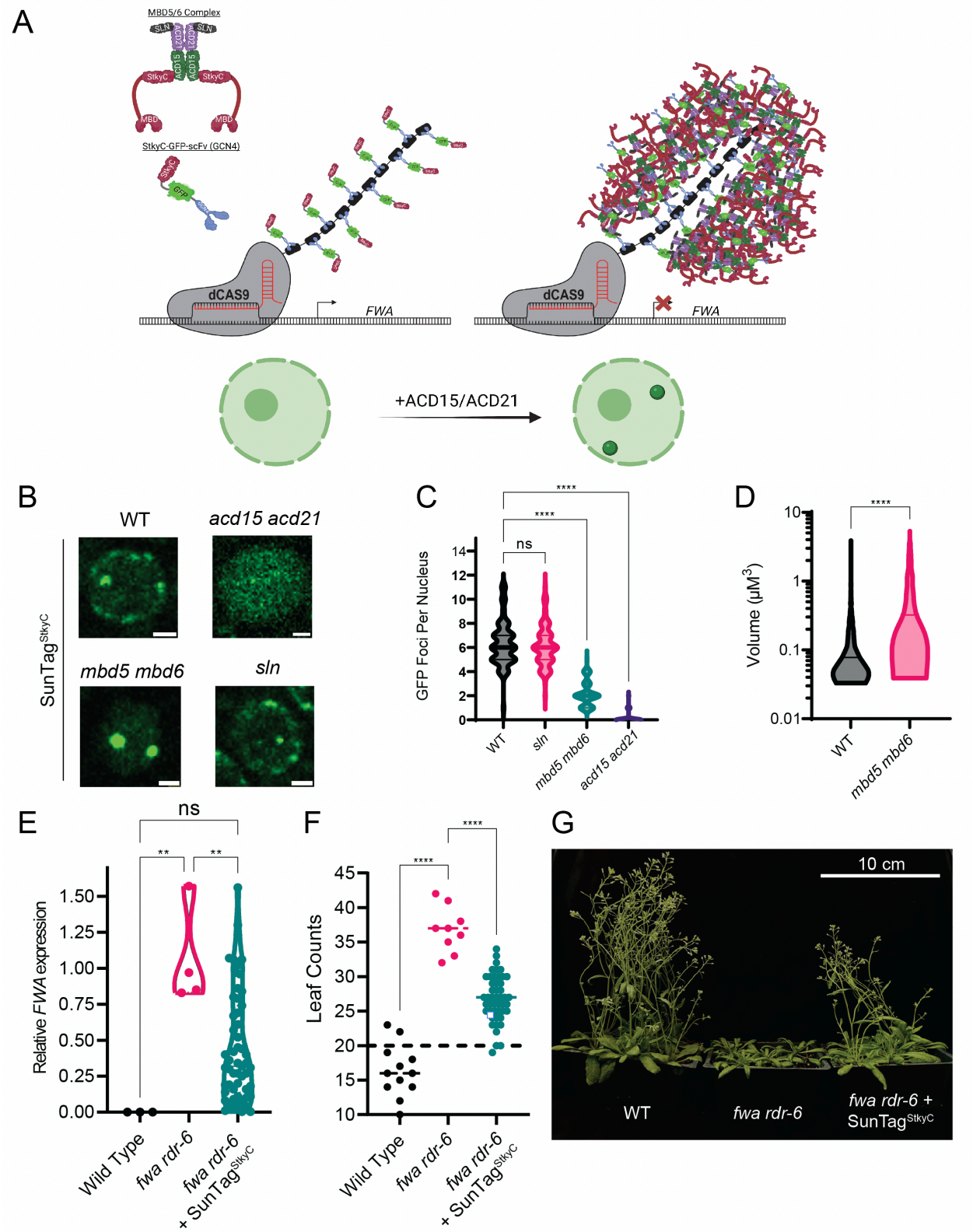

Fig. 5. ACD15 and ACD21 drive the formation of MBD5/6 multimeric assemblies. **(A)** Graphical representation of SunTag^{StkyC} system and the hypothesized result. Created with BioRender.com. **(B)** Representative nuclear images of SunTag^{StkyC} in different mutant backgrounds. **(C)** SunTag^{StkyC} GFP foci counts per nucleus (N=100 per genotype). Compared

using Welch's ANOVA Dunnett's T3 multiple comparisons test (****: P<0.0001, NS: P>=0.05). Scale bar = 2µM. **(D)** Volume of SunTag^{StkyC} GFP foci from 5 plant lines per genotype (WT: n=1461, *mbd5 mbd6*: n=1371). Two tailed t-test (****: P<0.0001, NS: P>=0.05). **(E)** RT-qPCR showing *FWA* expression in leaf tissue from T1 or control plants. Brown-Forsythe ANOVA with Tukey's multiple corrections test (**: P<0.01, NS: P>=0.05). **(F)** Leaf counts post flowering of T1 *fwa rdr-6* SunTag^{StkyC} plants. Brown-Forsythe ANOVA with Dunnett's multiple comparisons test (****: P<0.0001). **(G)** Representative image of early flowering T2 *fwa rdr-6* plants expressing SunTag^{StkyC}.